

Assignment 3 – Advanced Topics in First-Principles Electronic Structure Calculations

Sylvain Mortgat

May 18, 2025

The electronic structure of materials plays a fundamental role in determining their physical and chemical properties. In this work, three distinct studies are presented, each focusing on different aspects of electronic structure in three representative materials. All calculations are performed within the Kohn-Sham density functional theory (KS-DFT) framework, as implemented in the QUANTUM ESPRESSO package [1]. First, in Section 1, the electronic band structure and density of states (DoS) of magnesium oxide (MgO) in its face-centered cubic (FCC) phase are investigated. Its insulating behavior and ionic bonding is verified. Next, in Section 2, the influence of van der Waals (vdW) interactions on the structural relaxation of molybdenum disulfide (MoS₂) is explored. After determining the optimal lattice parameters, a comparative analysis of the band structures of bulk and monolayer MoS₂ is conducted, highlighting the role of dimensionality and interlayer interactions in modifying electronic properties. Finally, in Section 3, the geometric and magnetic stability of cobalt (Co) is studied. The equilibrium structure and magnetic ordering are examined to assess the stability of different configurations, providing insight into the material's behavior in bulk form.

1 Band Structure and Density of States of Magnesium Oxide

1.1 Methodology

Ground-state density The ground-state electronic density of the system is first computed using a self-consistent field (SCF) calculation. For both Mg and O atoms, 2.0.1 version scalar-relativistic norm-conserving pseudopotentials are employed, generated using the "atomic" code by A. Dal Corso v.5.0.99 svn rev. 10869. The lattice constant is set to 4.25 Å. The cutoff values for the calculations are selected based on recommendations from the SSFP Efficiency 1.3.0 library [2]. For Mg, the recommended wavefunction and charge density cutoffs are 30 Ry and 240 Ry, respectively, while for O they are 50 Ry and 400 Ry. The highest cutoff values among the constituent elements are selected, thus adopting the cutoffs for O (50 Ry for wavefunction and 400 Ry for charge density). A Monkhorst-Pack \vec{k} -point mesh of $8 \times 8 \times 8$ is employed for the SCF calculations [3]. The cutoff convergence is verified by monitoring the total energy: first, the density cutoff is fixed at 600 Ry while varying the wavefunction cutoff, then the wavefunction cutoff is held at 80 Ry while testing different density cutoffs.

Band structure For band structure calculations, a non-self-consistent field (NSCF) approach is implemented using the converged electron density and Kohn-Sham potential from the SCF calculation. The same cutoff values are maintained. The number of bands is determined based on the electron count in the unit cell provided by the SCF calculation; the SCF calculation indicates 8 valence electrons in the unit cell (2 from Mg and 6 from O), leading to the computation of 8 bands in the NSCF step. The remaining core electrons – 10 for Mg ($1s^2 2s^2 2p^6$) and 2 for O ($1s^2$) – are implicitly treated by the pseudopotentials. The \vec{k} -path for band structure calculations follows the high-symmetry points

W–L– Γ –X–W–K, where

$$W = \frac{2\pi}{a} \left(1, \frac{1}{2}, 0 \right), \quad L = \frac{2\pi}{a} \left(\frac{1}{2}, \frac{1}{2}, \frac{1}{2} \right), \quad \Gamma = (0, 0, 0),$$

$$X = \frac{2\pi}{a} (1, 0, 0), \quad K = \frac{2\pi}{a} \left(\frac{3}{4}, \frac{3}{4}, 0 \right).$$

This path is illustrated in Figure 1. To ensure adequate sampling along this path, 50 \vec{k} -points per unit of $2\pi/a$ are allocated, resulting in 35 points between W and L, 43 points between L and Γ , 50 points between Γ and X, 25 points between X and W, and 17 points between W and K.

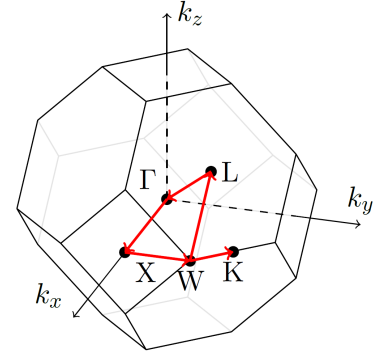


Figure 1: Brillouin zone of the FCC lattice. The high-symmetry path W–L– Γ –X–W–K used for the band structure calculation of MgO is highlighted in red.

Density of states The density of states (DoS) is computed through another NSCF calculation with a denser \vec{k} -mesh of $16 \times 16 \times 16$ using the tetrahedron method [4]. For a more detailed analysis, projected density of states (PDOS) calculations are performed to examine the relative contributions of particular atoms and orbitals to the total DoS, with special attention given to regions near the valence band maximum.

1.2 Results and Discussion

Convergence cutoffs The convergence behavior of FCC MgO's total energy with respect to wavefunction and density cutoffs is illustrated in Figure 2. The most precise calculation – with 80 Ry wavefunction cutoff and 650 Ry density cutoff – is used as the reference point. For the wavefunction cutoff, a monotonic decrease in energy difference is observed across the entire range of tested values. This convergence exhibits an approximately exponential decay for cutoffs below 45 Ry, followed by a plateau region between 45–60 Ry where energy differences stabilize around 1 mRy. Beyond 60 Ry, a further decrease in energy difference is noted. The convergence pattern for the density cutoff demonstrates a less regular behavior, with some oscillations at lower values. However, beyond 350 Ry, energy differences consistently remain within a narrow range between 0.5 μ Ry and 10 μ Ry, suggesting that convergence has been effectively achieved. These results confirm that the SSSP Efficiency recommended values of 50 Ry for wavefunction cutoff and 400 Ry for density cutoff provide balance between computational expense and numerical precision. From the SCF calculation, the highest occupied energy level is found to be 5.35 eV.

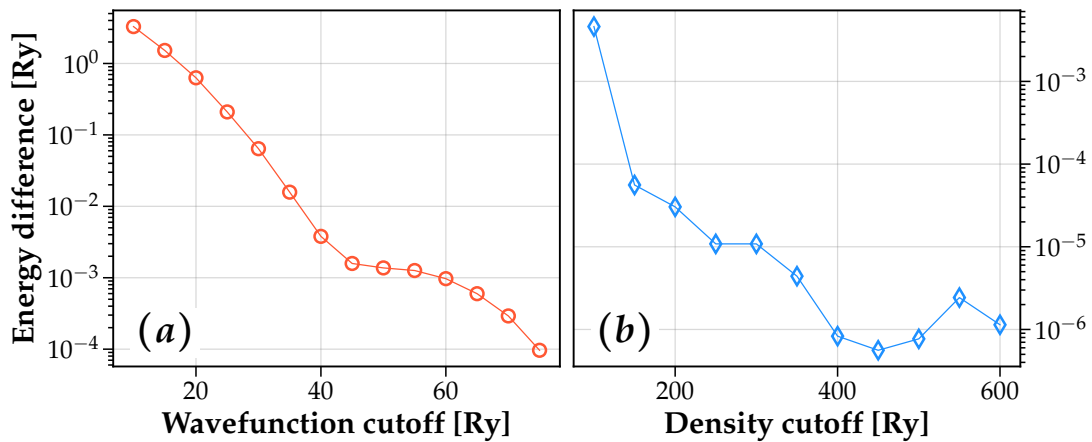


Figure 2: Total energy convergence tests for FCC MgO: (a) Wavefunction cutoff dependence (fixed density cutoff at 600 Ry), and (b) density cutoff dependence (fixed wavefunction cutoff at 80 Ry). Energy differences are computed relative to the most precise reference value (obtained at 80 Ry wavefunction cutoff and 650 Ry density cutoff).

Band structure, density of states and optical property of MgO Figure 3 displays the calculated band structure as well as the density and integrated density of states. It reveals a clear insulating character for MgO, with a band gap of 4.44 eV occurring at the Γ point. This result shows a 3.8% relative difference compared to the DFT-calculated value of 4.61 eV reported by Wang et al. [5].

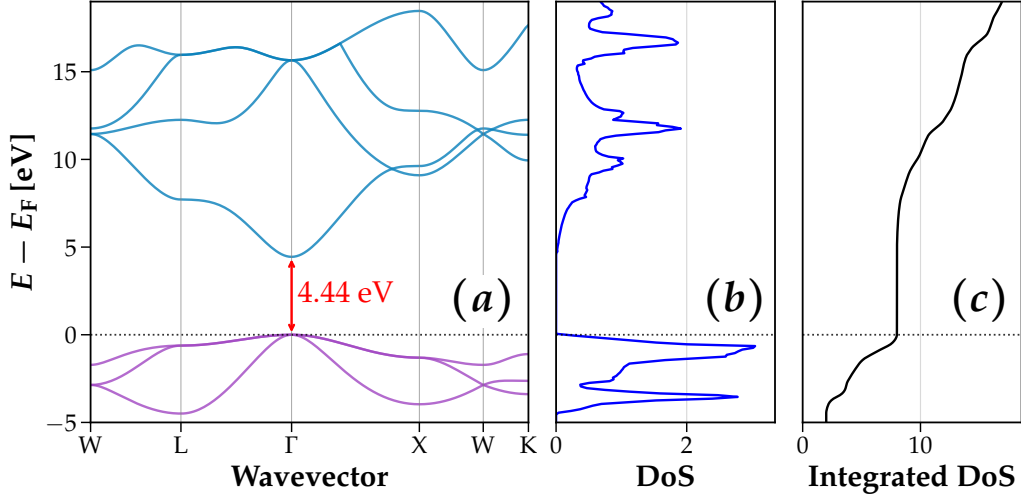


Figure 3: Electronic properties of FCC MgO with energies referenced to the Fermi level from the NSCF calculation. (a) Band structure along high-symmetry path W–L– Γ –X–W–K, revealing a direct band gap of 4.44 eV at Γ . (b) Total density of states. (c) Integrated density of states illustrating the cumulative electron count.

Qualitatively, the bands in our calculation appear steeper than those presented by Wang et al., with, for instance, greater curvature around Γ . As the effective mass of charge carriers is inversely proportional to this curvature ($m^* \propto (\partial^2 E / \partial k^2)^{-1}$), our results imply smaller effective masses for the charge carriers. While our calculated band gap aligns well with other DFT studies, it underestimates the experimental value of 7.90 eV by approximately 44%. This discrepancy between DFT calculations and experimental measurements is expected and stems from well-known limitations of standard DFT approaches. First, the Kohn-Sham band gap fundamentally differs from the true quasiparticle gap measured experimentally [6, 7]. Additionally, standard DFT functionals suffer from self-interaction errors and lack the derivative discontinuity in the exchange-correlation potential that properly accounts for the energy required to add or remove electrons from the system [8, 9]. Wang et al. demonstrates that applying the many-particle perturbation theory-based GW method yields a band gap of 6.06 eV, which is closer to the experimental value. Our calculated band gap of 4.44 eV establishes an absorption threshold for MgO, requiring incident photons to have at least this energy to promote electrons from the valence to the conduction band. This minimum energy corresponds to photons with wavelengths of 279 nm or shorter. This places MgO's absorption exclusively in the ultraviolet region of the electromagnetic spectrum. Hence, visible light lacks sufficient energy to bridge this gap, making MgO transparent to human vision. The experimental band gap of 7.90 eV would further restrict absorption to even higher-energy photons with

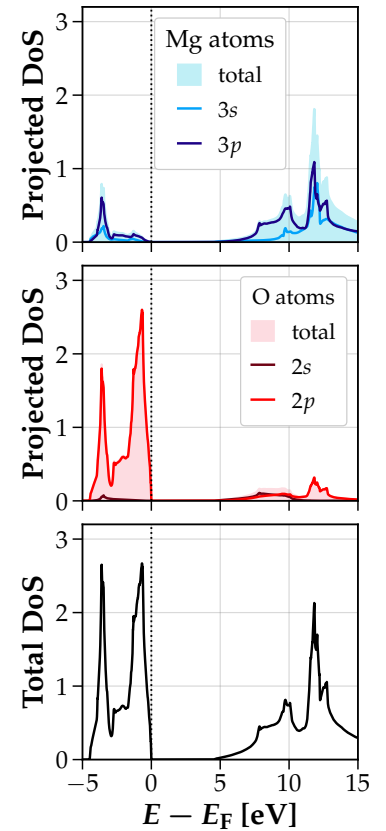


Figure 4: Projected and total DoS of FCC MgO. The valence band below E_F is dominated by O-2p states. Above E_F , the conduction band comprises primarily Mg-3s/3p states.

wavelengths below 157 nm. The calculated DoS (Fig. 3b) and its integrated form (Fig. 3c) provide complementary information to the band structure. The DOS exhibits a characteristic gap that exactly corresponds to the band gap observed in the band structure. It also shows a sharp increase at the valence band edge and a more gradual rise at the conduction band edge. Additional information can be extracted from the projected density of states illustrated in Figure 4. It reveals that the valence band is predominantly composed of O-2p states, while the conduction band is mainly derived from Mg-3s and 3p states. These results are consistent with those found by references [5, 10, 11]. This electronic structure is consistent with the ionic bonding character expected in MgO. The electronic configuration of isolated Mg atoms ($1s^2 2s^2 2p^6 3s^2$) and O atoms ($1s^2 2s^2 2p^4$) supports the interpretation that in crystalline MgO, Mg donates its two 3s electrons to O, resulting in Mg^{2+} and O^{2-} ions. This electron transfer is clearly reflected in the projected DoS, where the occupied O-2p states lie below the Fermi level, while the empty Mg-3s states are positioned above it. The minimal overlap between these states further confirms the predominantly ionic nature of the Mg-O bond, distinguishing it from covalent systems where significant orbital hybridization (overlap) is observed.

2 Molybdenum disulfide and van der Waals interactions

Layered materials exhibit distinctive structural characteristics. They feature strong chemical bonds between atoms within individual layers while neighboring layers are held together by weak, non-local, van der Waals interactions. These van der Waals have a decay proportional to r^{-6} . This non-locality necessitates the inclusion of non-local correlations in computational models. To account for these interactions, an additional term is incorporated into the exchange-correlation functional within the density functional theory framework.

2.1 Methodology

Geometry Optimization of MoS₂ The equilibrium lattice parameters of molybdenum disulfide (MoS₂) – the in-plane constant a and out-of-plane interlayer separation c – are determined through comparative density functional theory calculations. We contrast the standard Perdew-Burke-Ernzerhof (PBE) functional, which neglects van der Waals interactions, with the van der Waals-corrected VDW-DF2-C09 functional [12, 13, 14]. Initial optimization of a is performed with c fixed at the experimental value (12.30 Å), using a plane-wave basis set with 40 Ry wavefunction and 600 Ry charge density cutoffs, sampled on a $4 \times 4 \times 2$ \vec{k} -point mesh. The total energy near the minimum is fitted to the quadratic form $E(a) = \alpha + \beta(a - a_*)^2$ via the `lmfit` package [15], with parameter uncertainties reported as standard errors. Subsequent optimization of c is conducted with a fixed at the converged value a_* , following an identical protocol.

Band structure of Bulk MoS₂ The electronic band structure of bulk MoS₂ is computed using the optimized lattice parameters (a_* , c_*) obtained from structural relaxation. A SCF calculation is first performed on an $8 \times 8 \times 4$ \vec{k} -point mesh, maintaining the same plane-wave energy cutoffs (40 Ry for wavefunctions, 600 Ry for charge density) as in the geometry optimization. The band structure is then calculated non-self-consistently along the high-symmetry path K– Γ –M–K in the Brillouin zone, including 34 bands. The \vec{k} -point sampling follows the method of Section 1.1, with a uniform density of 47 points between K and Γ , 50 points between Γ and M, and 37 points between M and K.

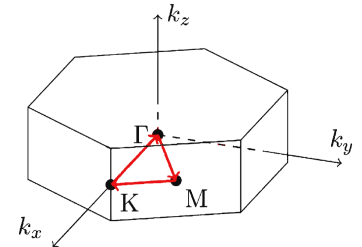


Figure 5: Brillouin zone of the HCP lattice. The high-symmetry path K– Γ –M–K–K used for the band structure calculation of MoS₂ is highlighted in red.

Monolayer MoS₂ band structure Single-layer MoS₂ is modeled by introducing vacuum separation between periodic images. To determine the appropriate interlayer distance for effectively isolating individual layers, an energy convergence study is performed with respect to vacuum thickness. Calculations employ an $8 \times 8 \times 1$ \vec{k} -point mesh and maintain the same cutoff parameters (40 Ry wavefunction, 600 Ry density) as the bulk system, with the reference state defined at $c/a_\star = 100$. The monolayer band structure is computed along the same path as for the bulk calculation, using identical \vec{k} -point sampling density. Due to the halved atom count (and consequently electronic states) in the monolayer unit cell, 17 bands are computed.

2.2 Results and Discussion

Geometry optimization The geometry optimization results are illustrated in Figure 6. They reveal distinct outcomes depending on whether van der Waals interactions are accounted for. Standard PBE calculations yield an optimized in-plane lattice parameter a_\star of (3.1976 ± 0.0001) Å, representing a 1.19% overestimation compared to the experimental value of $a_{\text{exp}} = 3.16$ Å.¹ The VDW-DF2-C09 functional produces $a_\star = (3.1568 \pm 0.0001)$ Å and $c_\star = (12.2579 \pm 0.0009)$ Å, deviating by only 0.1% and 0.34% from experimental values respectively. Although the interlayer separation energy curve appears more noisy than the in-plane variation, the global minimum remains identifiable. These results demonstrate that while standard PBE adequately describes intralayer bonding in MoS₂, explicit treatment of non-local van der Waals interactions is essential for accurate prediction of both in-plane and out-of-plane lattice parameters.

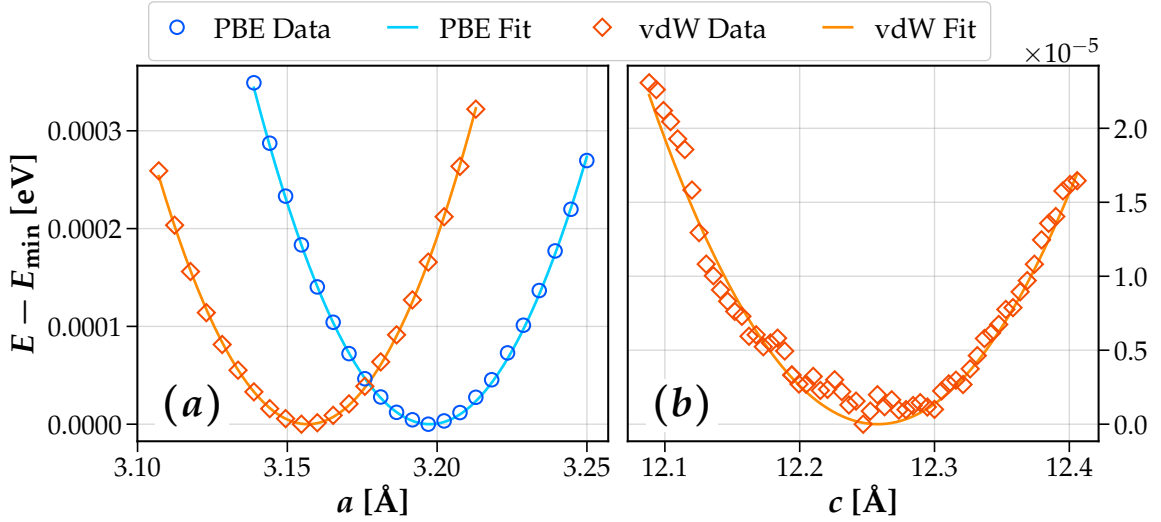


Figure 6: Energy minimization of (a) in-plane (a) and (b) out-of-plane (c) lattice parameters for bulk MoS₂ using PBE (blue) and vdW (orange) functionals. Solid lines show quadratic fits to the calculated energies. For easier comparison, all curves are shifted such that their minima, E_{min} , correspond to zero energy.

Band structures The band structure of bulk MoS₂, presented in Figure 7a, exhibits an indirect bandgap of approximately 0.82 eV, with the valence band maximum located along the Γ -M path and the conduction band minimum occurring along the Γ -K path. In contrast, the single-layer MoS₂ band structure, shown in Figure 7b, reveals a direct bandgap of approximately 1.78 eV, where both the valence band maximum and conduction band minimum are located at the K point. This transition

¹ While PBE calculations were performed for interlayer separation, the energy curve exhibited only monotonic decrease with increasing c/a ratio, preventing identification of a clear minimum. In contrast, VDW-DF2-C09 calculations yielded a clear energy minimum, enabling determination of c_\star .

from an indirect to a direct bandgap as the material is reduced from bulk to monolayer thickness represents an important transformation in the electronic properties of MoS₂. The change in band structure is attributed to quantum confinement, which modifies the hybridization of the orbitals between the S and Mo atoms [16, 17, 18]. The calculated monolayer bandgap value of 1.78 eV compares reasonably with experimentally reported values of approximately 1.9 eV at K [19]. For bulk MoS₂, the experimental indirect bandgap is reported as 1.2 eV [20], larger than our calculated value. It is also noted that in the literature, the bulk valence band maximum is typically observed at the Γ point rather than along the Γ -M path as calculated in this work [16, 21]. The conduction band minimum is more accurately reproduced, though it does not occur exactly at the midpoint between Γ and K.

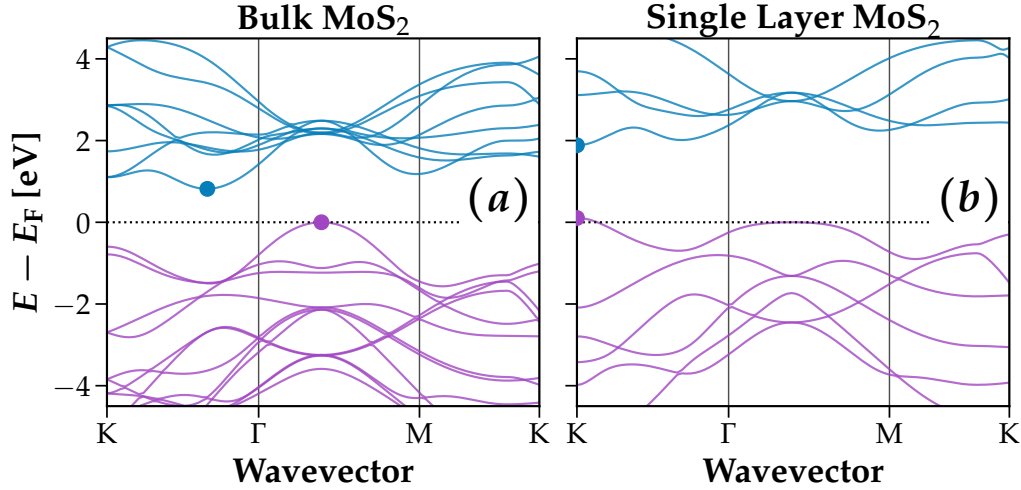


Figure 7: Electronic band structures of (a) bulk and (b) single-layer MoS₂ along the K- Γ -M-K high-symmetry path. The valence band maximum (purple circles) and conduction band minimum (teal circles) are marked, with the Fermi level set to 0 eV (dashed line). Bulk MoS₂ shows an indirect band gap of ~ 0.82 eV, while the single layer exhibits a larger direct gap at the K-point (~ 1.78 eV).

3 Phase Stability and Magnetism in Cobalt

This section investigates the correct geometric and magnetic ground state of cobalt using the PBE-GGA exchange-correlation functional.

3.1 Methodology

Comparing ferromagnetic FCC and HCP cobalt The relative stability of ferromagnetic FCC and HCP phases of cobalt is evaluated using SCF calculations. For both structures, experimental parameters from Nishizawa et al. [22] are employed: for FCC, the lattice constant is $a_{\text{FCC}} = 3.54$ Å, while for HCP, the parameters are $a_{\text{HCP}} = 2.50$ Å and $c = 4.06$ Å. All calculations use a wavefunction energy cutoff of 45 Ry and a charge density cutoff of 360 Ry. To account for the metallic nature of cobalt, where the Fermi level lies at a finite density of states, Marzari-Vanderbilt smearing [23] with a width of 0.01 Ry is applied.² The optimal initial magnetization is determined through a series of calculations in which this parameter varies between 0 and 1; the smallest value yielding consistent magnetic properties while minimizing the total energy is selected for further stability analysis. For reciprocal space sampling, the \vec{k} -point meshes for FCC ($12 \times 12 \times 12$) and HCP

² In QUANTUM ESPRESSO, the FCC structure uses `ibrav=2` while HCP uses `ibrav=4`. The spin-polarized calculations are performed by setting `nspin=2`.

$(12 \times 12 \times 6)$ are chosen to maintain nearly identical sampling densities in reciprocal space. For FCC, the primitive cell volume is $V_{\text{FCC}} = a_{\text{FCC}}^3/4$, while for HCP, it is $V_{\text{HCP}} = \sqrt{3}a_{\text{HCP}}^2c/2$. The Brillouin zone volume $\Omega = (2\pi)^3/V$ differs between the two structures, but the \vec{k} -point density $\rho = N/\Omega$, where $N = N_1 \times N_2 \times N_3$ is the total number of \vec{k} -points, is approximately matched with $\rho_{\text{FCC}} \approx 77.26 \text{ \AA}^{-3}$, and $\rho_{\text{HCP}} \approx 76.54 \text{ \AA}^{-3}$. The HCP mesh uses half as many points along k_z because the Brillouin zone is compressed in that direction. This arises because the reciprocal lattice vector $|\vec{b}_3| = 2\pi/c \approx 1.55 \text{ \AA}^{-1}$ is almost twice shorter than $|\vec{b}_1| = 4\pi/(\sqrt{3}a_{\text{HCP}}) \approx 2.90 \text{ \AA}^{-1}$ due to the elongated real-space c -axis ($c/a \approx 1.624$). Thus, fewer \vec{k} -points are needed along k_z to maintain a similar \vec{k} -point spacing. The complete expressions of the reciprocal lattice vectors are derived in the Appendix A.

Magnetic configurations in HCP Cobalt Following the determination of the geometric ground state, three possible magnetic configurations – ferromagnetic (FM), antiferromagnetic (AFM), and non-magnetic (NM) – are investigated. For the AFM case, oppositely signed starting magnetizations ($+m_{\text{start}}$ and $-m_{\text{start}}$) are assigned to the two cobalt atoms in the unit cell, maintaining all other computational parameters consistent with the ferromagnetic calculations. Analogous to the FM-HCP, the starting magnetization value is studied to identify the optimal value that simultaneously yields consistent magnetic properties and minimizes the total energy. Then, total energies for each magnetic phase are computed using SCF calculations. For the FM and NM phases, additional NSCF calculations are performed on finer \vec{k} -point grids of $18 \times 18 \times 9$ to compute the density of states using the tetrahedron method.

3.2 Results and Discussion

Starting Magnetizations for FM and AFM HCP Cobalt The starting magnetization is analyzed in Figure 8, and a clear transition is observed at a value of 0.1. Below this threshold, no magnetic behavior is exhibited by the system, with both total and absolute magnetizations approaching zero, while the total energy remains higher. For starting magnetizations exceeding 0.1, the total and absolute magnetizations are stabilized at consistent values, and the total energy is converged to its minimum. In the AFM configuration, a starting magnetization threshold of 0.05 is identified as sufficient for the establishment of the antiferromagnetic state. As expected for an antiferromagnetic system, there is no total magnetization, regardless of starting values. However, a distinct transition at 0.05 is observed in both the total energy and absolute magnetization, confirming successful convergence to the AFM state.

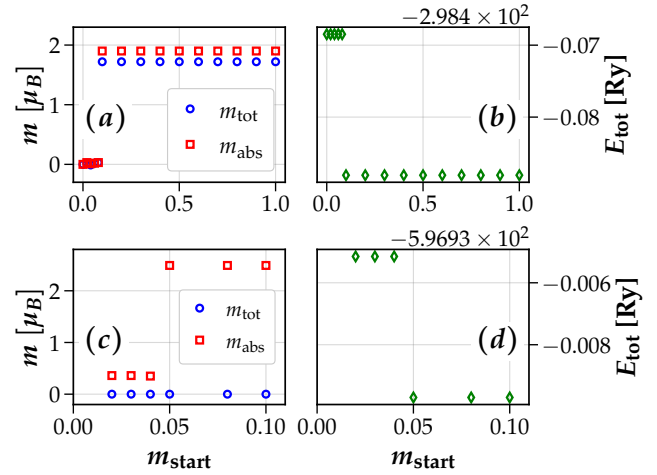


Figure 8: Dependence of total energy and magnetization (total and absolute) on initial spin polarization in (a–b) FM and (c–d) AFM configurations. Sharp transitions occur at 0.1 and 0.05 for FM and AFM phases, respectively.

Comparing ferromagnetic FCC and HCP Cobalt The relative stability of the FCC and HCP structures is examined through a direct comparison of total energies, which is normalized by the number of atoms per unit cell: two for HCP and one for FCC. An energy difference of approximately 20.7 mRy per atom is found between the structures, with the HCP phase being lower in energy and thus identified as the more stable configuration. This result is consistent with experimental

observations, where the HCP structure is known to be the ground state of cobalt at room temperature [24]. Both structures exhibit comparable magnetic behavior with a magnetic moment per atom of approximately $1.72 \mu_B$,³ indicating similar ferromagnetic character regardless of crystal structure. The obtained values are consistent with experimental [25] and DFT [26] results.

Magnetic configurations in HCP Cobalt The stability analysis reveals a clear energy hierarchy among the magnetic phases: $E_{NM} > E_{AFM} > E_{FM}$. Quantitatively, the energy differences are: $E_{AFM} - E_{FM} = 19.3$ mRy, $E_{AFM} - E_{NM} = 2.3$ mRy, and $E_{FM} - E_{NM} = 21.6$ mRy. The energy difference between AFM and NM phases is approximately one order of magnitude smaller than the differences between FM-NM or FM-AFM, highlighting the substantial energetic preference for the ferromagnetic state. The absolute magnetization calculations confirm the presence of local magnetic moments in both FM and AFM structures, with $1.89\mu_B$ per atom and $1.25\mu_B$ per atom, respectively.

Density of States of FM and NM phases The electronic density of states for non-magnetic and ferromagnetic phases of HCP cobalt is presented in Figure 9. In the non-magnetic configuration (Fig. 9a), a prominent peak is observed around the Fermi level with finite DoS. This is consistent with metallic behavior. For the ferromagnetic state (Fig. 9b), spin polarization is clearly visible, with distinct distributions for majority (spin-up) and minority (spin-down) electrons. When initialized with positive magnetization, the majority-spin DoS at E_F is significantly suppressed compared to the minority-spin channel, which exhibits a substantial peak at $E > E_F$. The integrated DoS reveals a higher occupation for majority spins relative to minority spins (3.29 states difference). Upon reversal of the initial magnetization (Fig. 9c), the spin channels are perfectly inverted. The finite DoS at E_F in all configurations confirms the metallic character of cobalt regardless of its magnetic state, while the spin asymmetry at the Fermi level in the ferromagnetic phase is indicative of its strong exchange splitting.

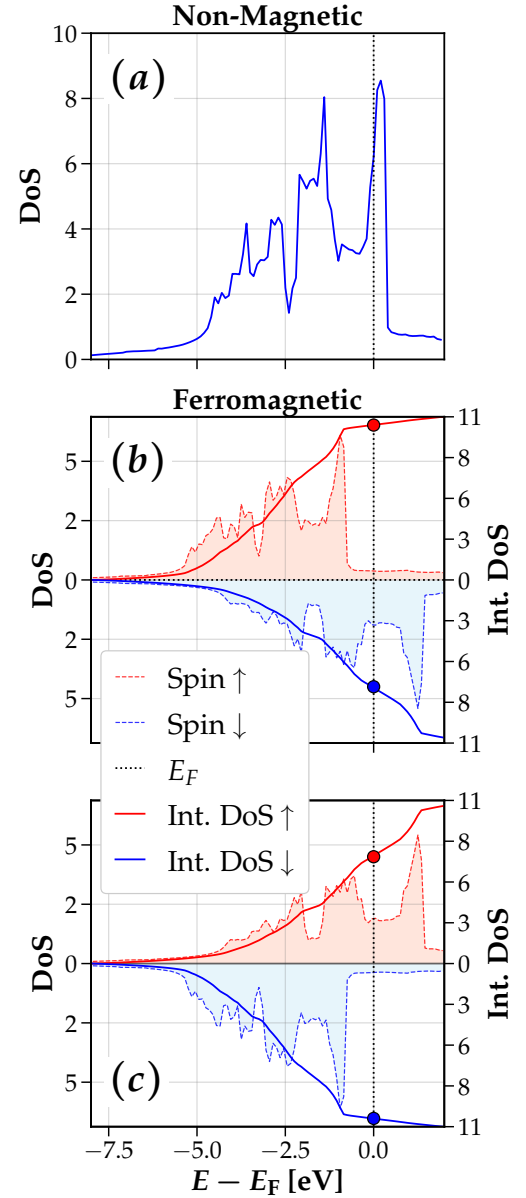


Figure 9: Electronic density of states of HCP cobalt. (a) Total DoS in the non-magnetic configuration. (b) Spin-resolved DoS (dashed lines) and integrated DoS (solid lines) for the ferromagnetic state, with majority (\uparrow) and minority (\downarrow) spin channels shown in red and blue, respectively. The vertical dotted line indicates the Fermi energy (E_F). (c) Same as (b), but calculated with spin-down initial magnetization.

³ μ_B indicates the Bohr magneton.

References

- [1] Paolo Giannozzi et al. “QUANTUM ESPRESSO: a modular and open-source software project for quantum simulations of materials”. In: *Journal of Physics: Condensed Matter* 21.39 (Sept. 2009), p. 395502. ISSN: 1361-648X. DOI: [10.1088/0953-8984/21/39/395502](https://doi.org/10.1088/0953-8984/21/39/395502). URL: <http://dx.doi.org/10.1088/0953-8984/21/39/395502>.
- [2] Gianluca Prandini et al. “Precision and efficiency in solid-state pseudopotential calculations”. In: *npj Computational Materials* 4.1 (2018). <http://materialscloud.org/sssp>, p. 72. ISSN: 2057-3960. DOI: [10.1038/s41524-018-0127-2](https://doi.org/10.1038/s41524-018-0127-2). URL: <https://www.nature.com/articles/s41524-018-0127-2>.
- [3] Hendrik J. Monkhorst and James D. Pack. “Special points for Brillouin-zone integrations”. In: *Phys. Rev. B* 13 (12 June 1976), pp. 5188–5192. DOI: [10.1103/PhysRevB.13.5188](https://doi.org/10.1103/PhysRevB.13.5188). URL: <https://link.aps.org/doi/10.1103/PhysRevB.13.5188>.
- [4] Peter E. Blöchl, O. Jepsen, and O. K. Andersen. “Improved tetrahedron method for Brillouin-zone integrations”. In: *Phys. Rev. B* 49 (23 June 1994), pp. 16223–16233. DOI: [10.1103/PhysRevB.49.16223](https://doi.org/10.1103/PhysRevB.49.16223). URL: <https://link.aps.org/doi/10.1103/PhysRevB.49.16223>.
- [5] Jia Wang et al. “Theoretical investigation of the electronic structure and optical properties of zinc-doped magnesium oxide”. In: *J. Comput. Electron.* 15.4 (Dec. 2016), pp. 1521–1530. ISSN: 1569-8025. DOI: [10.1007/s10825-016-0906-2](https://doi.org/10.1007/s10825-016-0906-2). URL: <https://doi.org/10.1007/s10825-016-0906-2>.
- [6] E. J. Baerends, O. V. Gritsenko, and R. van Meer. “The Kohn–Sham gap, the fundamental gap and the optical gap: the physical meaning of occupied and virtual Kohn–Sham orbital energies”. In: *Phys. Chem. Chem. Phys.* 15 (39 2013), pp. 16408–16425. DOI: [10.1039/C3CP52547C](https://doi.org/10.1039/C3CP52547C). URL: <http://dx.doi.org/10.1039/C3CP52547C>.
- [7] E. J. Baerends. “From the Kohn–Sham band gap to the fundamental gap in solids. An integer electron approach”. In: *Phys. Chem. Chem. Phys.* 19 (24 2017), pp. 15639–15656. DOI: [10.1039/C7CP02123B](https://doi.org/10.1039/C7CP02123B). URL: <http://dx.doi.org/10.1039/C7CP02123B>.
- [8] John P. Perdew. “Density functional theory and the band gap problem”. In: *International Journal of Quantum Chemistry* 28.S19 (1985), pp. 497–523. DOI: <https://doi.org/10.1002/qua.560280846>. eprint: <https://onlinelibrary.wiley.com/doi/pdf/10.1002/qua.560280846>. URL: <https://onlinelibrary.wiley.com/doi/abs/10.1002/qua.560280846>.
- [9] Gregor Michalicek (<https://physics.stackexchange.com/users/166799/gregor-michalicek>). *Why does Density Functional Theory (DFT) underestimate bandgaps?* Physics Stack Exchange. (version: 2021-03-28). eprint: <https://physics.stackexchange.com/q/360454>. URL: <https://physics.stackexchange.com/q/360454>.
- [10] Shigemi Kohiki et al. “Energy Loss Structure of X-ray Photoelectron Spectra of MgO and α -Al₂O₃”. In: *The Journal of Physical Chemistry B* 103.25 (June 1999), pp. 5296–5299. DOI: [10.1021/jp9901996](https://doi.org/10.1021/jp9901996). URL: <https://doi.org/10.1021/jp9901996>.
- [11] P. D. C. King et al. “Valence-band electronic structure of CdO, ZnO, and MgO from x-ray photoemission spectroscopy and quasi-particle-corrected density-functional theory calculations”. In: *Phys. Rev. B* 79 (20 May 2009), p. 205205. DOI: [10.1103/PhysRevB.79.205205](https://doi.org/10.1103/PhysRevB.79.205205). URL: <https://link.aps.org/doi/10.1103/PhysRevB.79.205205>.
- [12] M. Dion et al. “Van der Waals Density Functional for General Geometries”. In: *Phys. Rev. Lett.* 92 (24 June 2004), p. 246401. DOI: [10.1103/PhysRevLett.92.246401](https://doi.org/10.1103/PhysRevLett.92.246401). URL: <https://link.aps.org/doi/10.1103/PhysRevLett.92.246401>.

- [13] Valentino R. Cooper. “Van der Waals density functional: An appropriate exchange functional”. In: *Phys. Rev. B* 81 (16 Apr. 2010), p. 161104. DOI: [10.1103/PhysRevB.81.161104](https://doi.org/10.1103/PhysRevB.81.161104). URL: <https://link.aps.org/doi/10.1103/PhysRevB.81.161104>.
- [14] Kyuho Lee et al. “Higher-accuracy van der Waals density functional”. In: *Phys. Rev. B* 82 (8 Aug. 2010), p. 081101. DOI: [10.1103/PhysRevB.82.081101](https://doi.org/10.1103/PhysRevB.82.081101). URL: <https://link.aps.org/doi/10.1103/PhysRevB.82.081101>.
- [15] Matthew Newville et al. *LMFIT: Non-Linear Least-Squares Minimization and Curve-Fitting for Python*. Version 1.3.3. Mar. 2025. DOI: [10.5281/zenodo.15014437](https://doi.org/10.5281/zenodo.15014437). URL: <https://doi.org/10.5281/zenodo.15014437>.
- [16] Qing Hua Wang et al. “Electronics and optoelectronics of two-dimensional transition metal dichalcogenides”. In: *Nature Nanotechnology* 7.11 (2012), pp. 699–712. ISSN: 1748-3395. DOI: [10.1038/nnano.2012.193](https://doi.org/10.1038/nnano.2012.193). URL: <https://doi.org/10.1038/nnano.2012.193>.
- [17] Andrea Splendiani et al. “Emerging Photoluminescence in Monolayer MoS₂”. In: *Nano Letters* 10.4 (2010), pp. 1271–1275. ISSN: 1530-6984. DOI: [10.1021/nl903868w](https://doi.org/10.1021/nl903868w). URL: <https://doi.org/10.1021/nl903868w>.
- [18] Dipankar Saha and Peter Kruse. “Editors’ Choice—Review—Conductive Forms of MoS₂ and Their Applications in Energy Storage and Conversion”. In: *Journal of The Electrochemical Society* 167.12 (Sept. 2020), p. 126517. DOI: [10.1149/1945-7111/abb34b](https://doi.org/10.1149/1945-7111/abb34b). URL: <https://dx.doi.org/10.1149/1945-7111/abb34b>.
- [19] Kin Fai Mak et al. “Atomically Thin MoS₂: A New Direct-Gap Semiconductor”. In: *Phys. Rev. Lett.* 105 (13 Sept. 2010), p. 136805. DOI: [10.1103/PhysRevLett.105.136805](https://doi.org/10.1103/PhysRevLett.105.136805). URL: <https://link.aps.org/doi/10.1103/PhysRevLett.105.136805>.
- [20] Manish Chhowalla et al. “The chemistry of two-dimensional layered transition metal dichalcogenide nanosheets”. In: *Nature Chemistry* 5.4 (2013), pp. 263–275. ISSN: 1755-4349. DOI: [10.1038/nchem.1589](https://doi.org/10.1038/nchem.1589). URL: <https://doi.org/10.1038/nchem.1589>.
- [21] Sarmistha Das, Gayatri Swain, and Kulamani Parida. “One Step Towards the 1T/2H-MoS₂ Mixed Phase: A Journey from Synthesis to Application”. In: *Materials Chemistry Frontiers* 5.5 (2021), pp. 2143–2172. DOI: [10.1039/D0QM00802H](https://doi.org/10.1039/D0QM00802H). URL: <http://dx.doi.org/10.1039/D0QM00802H>.
- [22] T. Nishizawa and K. Ishida. “The Co (Cobalt) system”. In: *Bulletin of Alloy Phase Diagrams* 4.4 (1983), pp. 387–390. ISSN: 0197-0216. DOI: [10.1007/BF02868089](https://doi.org/10.1007/BF02868089). URL: <https://doi.org/10.1007/BF02868089>.
- [23] Nicola Marzari et al. “Thermal Contraction and Disordering of the Al(110) Surface”. In: *Phys. Rev. Lett.* 82 (16 Apr. 1999), pp. 3296–3299. DOI: [10.1103/PhysRevLett.82.3296](https://doi.org/10.1103/PhysRevLett.82.3296). URL: <https://link.aps.org/doi/10.1103/PhysRevLett.82.3296>.
- [24] T. Kaneko and T. Kanomata. “Magnetic Properties of d-Elements, Alloys and Compounds Under Pressure · 2.4 ε-Co: Datasheet from Landolt-Börnstein - Group IV Physical Chemistry · Volume 22A”. In: *Magnetic Properties of d-Elements, Alloys and Compounds Under Pressure*. Ed. by Y. Kawazoe, T. Kaneko, and Y. Uwatoko. Vol. 22A. Landolt-Börnstein - Group IV Physical Chemistry. Part of SpringerMaterials. Springer-Verlag Berlin Heidelberg, 2014. DOI: [10.1007/978-3-642-41834-1_5](https://doi.org/10.1007/978-3-642-41834-1_5). URL: https://materials.springer.com/lb/docs/sm_lbs_978-3-642-41834-1_5 (visited on 05/17/2025).
- [25] Isabelle M.L. Billas, A. Châtelain, and Walt A. de Heer. “Magnetism of Fe, Co and Ni clusters in molecular beams”. In: *Journal of Magnetism and Magnetic Materials* 168.1 (1997), pp. 64–84. ISSN: 0304-8853. DOI: [https://doi.org/10.1016/S0304-8853\(96\)00694-4](https://doi.org/10.1016/S0304-8853(96)00694-4). URL: <https://www.sciencedirect.com/science/article/pii/S0304885396006944>.

- [26] A. Lekdadri et al. “First-principle study of electronic and magnetic properties in cobalt-niobium alloys”. In: *Materials Today: Proceedings* 37 (2021). The International Conference on Water Depollution and Green Energy 2019, pp. 3813–3820. ISSN: 2214-7853. DOI: <https://doi.org/10.1016/j.matpr.2020.08.261>. URL: <https://www.sciencedirect.com/science/article/pii/S2214785320361319>.

A Reciprocal Lattice Vectors

The primitive vectors of the HCP structure, with in-plane parameter a and out-of-plane parameter c , are given by

$$\vec{a}_1 = (a, 0, 0), \quad \vec{a}_2 = \left(\frac{a}{2}, \frac{\sqrt{3}a}{2}, 0\right), \quad \vec{a}_3 = (0, 0, c).$$

The reciprocal lattice vectors are then deduced from the relation $\vec{a}_i \cdot \vec{b}_j = 2\pi\delta_{ij}$. This gives a set of nine equations:

$$\left\{ \begin{array}{ll} \vec{a}_1 \cdot \vec{b}_1 = ab_{1x} = 2\pi & \implies b_{1x} = \frac{2\pi}{a} \\ \vec{a}_2 \cdot \vec{b}_1 = \frac{a}{2}b_{1x} + \frac{\sqrt{3}a}{2}b_{1y} = 0 & \implies b_{1y} = -\frac{2\pi}{\sqrt{3}a} \\ \vec{a}_3 \cdot \vec{b}_1 = cb_{1z} = 2\pi & \implies b_{1z} = 0 \\ \vec{a}_1 \cdot \vec{b}_2 = ab_{2x} = 0 & \implies b_{2x} = 0 \\ \vec{a}_2 \cdot \vec{b}_2 = \frac{a}{2}b_{2x} + \frac{\sqrt{3}a}{2}b_{2y} = 2\pi & \implies b_{2y} = \frac{4\pi}{\sqrt{3}a} \\ \vec{a}_3 \cdot \vec{b}_2 = cb_{2z} = 0 & \implies b_{2z} = 0 \\ \vec{a}_1 \cdot \vec{b}_3 = ab_{3x} = 0 & \implies b_{3x} = 0 \\ \vec{a}_2 \cdot \vec{b}_3 = \frac{a}{2}b_{3x} + \frac{\sqrt{3}a}{2}b_{3y} = 0 & \implies b_{3y} = 0 \\ \vec{a}_3 \cdot \vec{b}_3 = cb_{3z} = 0 & \implies b_{3z} = \frac{2\pi}{c} \end{array} \right.$$

Therefore, the reciprocal lattice vectors are

$$\vec{b}_1 = \left(\frac{2\pi}{a}, -\frac{2\pi}{\sqrt{3}a}, 0\right), \quad \vec{b}_2 = \left(0, \frac{4\pi}{\sqrt{3}a}, 0\right), \quad \vec{b}_3 = \left(0, 0, \frac{2\pi}{c}\right),$$

with corresponding norms

$$|\vec{b}_1| = |\vec{b}_2| = \frac{4\pi}{\sqrt{3}a}, \quad |\vec{b}_3| = \frac{2\pi}{c}.$$